JOURNAL OF PROPULSION AND POWER
Vol. 17, No. 5, September–October 2001

Heating and Plasma Properties in a Coaxial Gasdynamic Pulsed Plasma Thruster

Stewart S. Bushman* and Rodney L. Burton†
University of Illinois at Urbana–Champaign, Urbana, Illinois 61801

Multiple experimental diagnostics are used to characterize a coaxial pulsed plasma thruster (PPT-4). Operating at a capacitor-stored energy E_0 of 9 J, thermocouple data indicate that half of the energy that reaches the PPT is lost as heat to the walls. Thrust-stand measurements yield an impulse bit of 29 ± 2 μN · s/J, corresponding to an I_{sp} of 745 ± 45 s and a thruster efficiency of $10.6 \pm 1.3\%$. Quadruple electrostatic probe measurements indicate a symmetric plume with a peak electron density of $4.2 \pm 1.0 \times 10^{13}$ cm^{-3} and an initial electron temperature of 2.0 ± 0.3 eV. The ion Mach number u_i/c_m is generally supersonic with a value of 3.0 ± 0.5. When the arrival time of peak n_e is measured, an ion velocity of 34 km/s is indicated. A magnetic probe survey was used to measure magnetic field strength and identify enclosed current contours.

Nomenclature

A	=	probe surface area
A_{enc}	=	enclosed single B-probe coil area
B	=	magnetic field
c_m	=	most probable ion thermal speed
E_0	=	stored capacitor energy
I_{sp}	=	specific impulse
Kn	=	Knudsen number
k	=	Boltzmann's constant
l_B	=	path length of constant B field
m	=	mass loss per pulsed plasma thruster pulse
$\bar{m}_i$	=	average ion mass
n	=	number of coils in B probe
n_e	=	electron number density
n_i	=	ion number density
n_n	=	neutral number density
P_n	=	designation of probe n
$\dot{Q}$	=	heating power
T_e	=	electron temperature
T_i	=	ion temperature
u_i	=	ion velocity
V_{d2}	=	P_1 and P_2 potential difference
V_{d3}	=	P_1 and P_3 potential difference
x_i	=	wake effect collection parameter
γ	=	ratio of specific heats
ε_0	=	permittivity constant
η_h	=	heating efficiency
η_t	=	thruster efficiency
η_{tr}	=	transfer efficiency
λ_{a-b}	=	mean free path between a and b
λ_D	=	debye length
λ_{mfp}	=	mean free path
μ_0	=	permeability constant
ν	=	pulse frequency
ϕ	=	integrated B-probe signal, e/kT_e
Ω	=	Hall parameter

Received 14 July 2000; revision received 1 June 2001; accepted for publication 15 June 2001.

*M.S. Candidate, Department of Aeronautical and Astronautical Engineering; currently Research Scientist, W.E. Research, 4360 San Juan Court, Rosamond, CA 93560.

†Professor, Department of Aeronautical and Astronautical Engineering. Associate Fellow AIAA.

Introduction

THE solid-propellant pulsed plasma thruster (PPT) has a 35-year history of space operation, beginning in 1964 with the Soviet Zond-2 mission.[1,2] By providing a train of small, discrete impulse bits, PPTs are ideal for such diverse applications as orbit raising,[3] drag makeup,[4] attitude control,[5] constellation stationkeeping,[6] and deep-space missions.[7]

Teflon®-fed PPTs are especially well suited for low-thrust, on-board propulsion because they use a nontoxic propellant and are highly reliable, solid state, low power, and lightweight, inasmuch as they require no propellant storage system.[8] Additionally, because the thruster energy and pulse frequency are variable, PPTs are highly throttlable.

PPTs also have a history of low operational efficiency, generally measured to be in the sub-10% range.[2] This characteristic of PPTs is largely due to both inefficient propellant utilization and poor energy efficiency due to transfer and thermal losses.[9] A primary goal of PPT research is to minimize these losses to make the thruster a more attractive option for future missions.

In a traditional rectangular, breech-fed PPT, a spark induces a capacitor discharge arc across the face of a Teflon bar. Heat from the arc evaporates the Teflon, which is then accelerated electromagnetically and gasdynamically out of a nozzle. As the fuel is expended, more is advanced forward by a constant-force spring.[2]

Several characteristics of rectangular PPT operation complicate the understanding of this process significantly. The geometry leads to edge effects, current gradients, and magnetic field asymmetry in the discharge.[10] Modeling this has proven especially difficult.[11] Spark plug operation can result in shot-to-shot variation in PPT performance. Two acceleration mechanisms are present in the PPT discharge, electrothermal (ET) and electromagnetic (EM), each interacting in wholly different ways with the plasma.[2] Despite the difficulties in deciphering exactly how the PPT operates, it is a proven, flight-qualified, and flight-tested technology.

Over the past three decades, several different PPT configurations have been investigated, exploring changes as minor as flared electrodes[12] to side-fed fuel bars[13] to a coaxial geometry[14] to combinations of these options: side fed with flared electrodes[13] and coaxial geometry with side-fed bars.[15,16] This last, side-fed, coaxial configuration is the baseline PPT for the research presented here.[17] A schematic is provided in Fig. 1.

The operation for this coaxial geometry is similar to a rectangular PPT. A cavity is formed by the intersection of two Teflon bars held up against a central anode and two nonablating boron nitride insulators. The anode is raised to a given potential by charging the capacitor. The igniter plug, mounted in a boron nitride nozzle, fires, resulting in an arc discharge between the anode and the annular cathode at

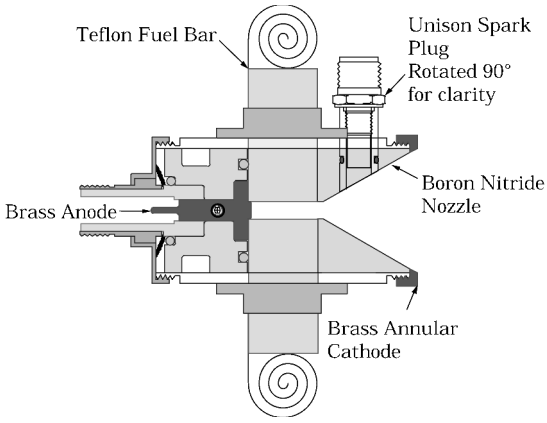

Fig. 1 Detailed schematic of PPT-4; in capillary mode, side bars are replaced with a Teflon cylinder.

the end of the nozzle. It is possible to modify PPT-4 to support four side-fed bars. Alternatively, a Teflon cylinder can be used in a capillary mode to simulate a four-bar feed system.

In addition to the geometrical changes from the traditional PPT, the circuit has been modified. A diode has been installed across the terminals of the capacitors, preventing current reversal in the circuit and resulting in a unipolar current pulse. This current form is advantageous because it prevents a $\boldsymbol{j} \times \boldsymbol{B}$ field from accelerating propellant into the PPT, and it helps extend capacitor life by excluding it from the circuit after the first half-cycle.

These changes have resulted in a PPT performance regime that is primarily ET. Arc heating from a ~10-J pulse produces a hot, high-pressure plasma inside the cavity that is released as a rarefaction wave moves from the nozzle throat to the anode face.[2] Experiments with the coaxial PPT geometry have resulted in the present iteration, PPT-4.

The cavity provides a small, enclosed volume where the vaporized Teflon is heated and pressurized by the arc and then expelled into a diverging nozzle, where it expands and accelerates, further increasing the exit velocity of the plasma. Because the current pulse is nonreversing, the net electromagnetic force, $\boldsymbol{F}_{\mathrm{EM}} = \boldsymbol{j} \times \boldsymbol{B}$, is directed exclusively out of the PPT, maximizing that impulse component.

Experimental Apparatus

PPT-4 possesses an annular brass cathode with an inner diameter of 43 mm and a boron nitride (BN) nozzle with a 30-deg half-angle and an area ratio of 46:1. The igniter plug is a semiconductor-type aircraft combustor spark plug, side mounted in the nozzle. Teflon bars (25.4 mm long × 6.4 mm thick) are held firmly against the 4.8-mm-diam center anode by constant-force springs. Completing the cavity are two D-shaped pieces of BN. The center electrode (anode) comprises a 4.8-mm-diam threaded brass rod that can provide a variable cavity length.

Two diagnostics, a voltage probe and a Rogowski coil, are mounted in the back insulator. The thruster was designed to connect to a capacitive pulse-forming network (PFN) via a 2-cm-long × 1-cm-diam coaxial steel and copper stub connector.

The PFN consists of four 2-μF, oil-filled, high-voltage capacitors connected in parallel. Ring-down and PSpice[18] current matching yield an equivalent series resistance of 7.5 mΩ and net inductance of 13 nH for the entire PFN. Two diodes have been placed across the terminals of each capacitor, resulting in zero PPT current reversal during the pulse. PSpice matching of the PPT current pulse at 9 J yields the external inductance $L_{\mathrm{ext}} = 82$ nH and the arc impedance $Z_{\mathrm{PPT}} = 54$ mΩ. The transmission line resistance is estimated to be 1 mΩ. The PPT-4 circuit schematic is shown in Fig. 2.

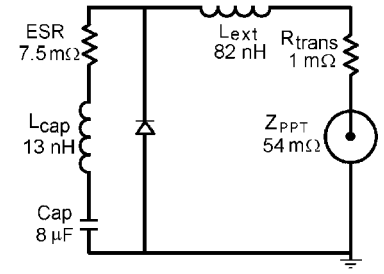

Fig. 2 PPT-4 circuit schematic from PSpice matching.

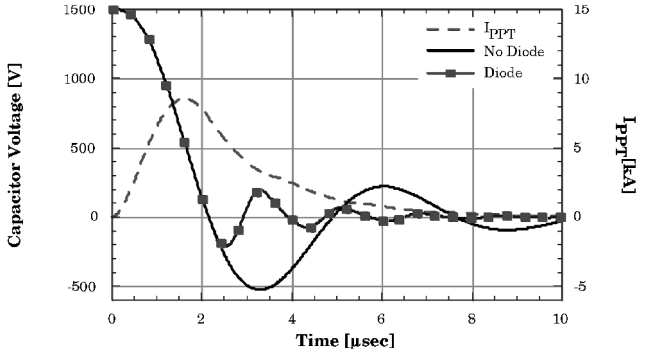

Fig. 3 Effect of diode on capacitor voltage reversal predicted by circuit modeling; diode reduces voltage reversal from 33 to 13%.

Thruster Life

New propellant bars inserted into the thruster undergo a burn-in phase whereupon the operation of the PPT reshapes the cavity into a steady-state shape that leaves a significant portion of the BN exposed to the arc, permitting loss of energy by heat transfer to the nonablative material.

With a cylinder of Teflon used to yield a capillary mode of operation, the entire cavity is composed of Teflon with no exposed insulation. However, additional fuel is not being fed into the system, so that no steady-state shape arises. The cylinder simply bores out until the fuel is expended. Observations of this ablation indicate that it occurs evenly over the cylinder.

A typical PPT mission lifetime is required to be some 20 million pulses during on-orbit operation.[19] Of primary concern is whether or not the capacitors, the igniter plug, and the electrodes are capable of withstanding the rigors of constant firing for long periods of time. Capacitor life is shortened every time there is voltage on the terminals. When the diode is put in the PPT circuit, the capacitor voltage and current are zero after the first-quarter cycle, thus reducing the stress on the capacitor.

Circuit modeling (Fig. 3) indicates that voltage ringing is not totally eliminated in the capacitor, but the magnitude is reduced significantly. The voltage reversal with no diode is 33% and with the diode is 13%. The stress on the capacitor is proportional to V^2, hence, the imparted stress reversal for the diode case is six times less than if there is no diode installed. To further extend capacitor life, a diode can also be added in series with the capacitor to eliminate voltage reversal completely.

Metal erosion and carbon deposition are other processes that serve to reduce PPT life. PPT-4 has been fired successfully for ~70,000 shots with little evidence of ash accumulation on the plug, which is observed to have a clean tip. Minimal arc scoring is observed on the steel igniter plug exterior, but no discernible metal has been eroded.

Similarly, the brass electrodes have exhibited little evidence of metal erosion during the testing of PPT-4. Far more significant is the carbon deposition that completely blackens the exposed face of the central electrode and the chamfered part of the front electrode that completes the nozzle cone.

Thrust Mode

The EM and ET thrust impulse of PPT-4 can be written as

$$I_{\mathrm{bit}} = \tfrac{1}{2} L' \Psi + I_{\mathrm{ET}} \tag{1}$$

where L' is the inductance gradient, calculated from the PPT geometry, and

$$\Psi = \int I^2 \, \mathrm{d}t$$

For a coaxial thruster, assuming the current density is axisymmetric, L' is a function of the inner radius of the annular electrode r_a and the radius of the central electrode r_c (Refs. 1 and 2):

$$L'[H/m] = (\mu_0/2\pi)\left[\ln(r_a/r_c) + \tfrac{3}{4}\right] \tag{2}$$

For PPT-4, $L' = 0.59$ μH/m. For the PPT-4 current pulse, $\Psi = 115.1$ A·s. This yields $I_{EM} = 4$ μN·s/J. When this result is combined with the measured impulse bit from this effort, $I_{bit} = 29$ μN·s/J, an ET, or gasdynamic, impulse bit of 25 μN·s/J is given. This ET contribution is dominated by the pressure force on the anode created by the ohmic heating of the ablated mass. Clearly, PPT-4 is dominated by the gasdynamic impulse component that comprises 86% of the total impulse bit.

Plasma Diagnostics

The PPT exhausts into a 1-m-diam × 1.5-m-long vacuum tank, held at vacuum by a 1500 l/s turbomolecular pump that provides a typical operating environment of 30 μtorr. Two types of plasma probes were used in this research: a quadruple electrostatic probe and a magnetic probe. The probes were mounted on a linear translation carriage.[20]

The PPT centerline is defined as the z axis in cylindrical coordinates. Positive z is measured from the downstream face of the annular electrode (cathode). Radial distance from centerline is denoted by r, and θ is measured from the spark plug location, which corresponds to $\theta = 0$.

The quadruple probe used here, derived from a previous design,[20] consists of three 0.3-mm-diam × 2.3-mm-long cylindrical tungsten probes (P_1, P_2, and P_3), which are aligned parallel to the flow velocity, and one 0.3 mm-diam × 2.5-mm-long tungsten probe (P_4), which is perpendicular to the flow. The probes are mounted in a round, quad-bore, insulating alumina (Al_2O_3) tube (3.2 mm o.d. × 0.5 mm i.d.). A quadruple probe schematic is in Fig. 4.

The detailed magnetic field strength distribution in the nozzle and plume of PPT-4 is measured with a magnetic probe (B-probe),[21] pictured in Fig. 5, consisting of four turns of 30-gauge magnet wire shielded in Pyrex™. The wire leads are tightly twisted to minimize extraneous field collection area and fed through single-bore alumina tubing into a thermocouple fitting identical to that of the quadruple probe. Integrating the raw B-probe voltage signal ($V = \mathrm{d}\phi/\mathrm{d}t$) gives B_θ.

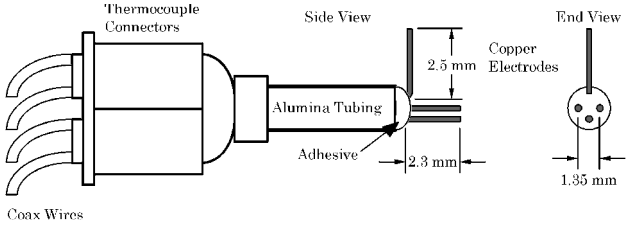

Fig. 4 Quadruple electrostatic probe schematic.

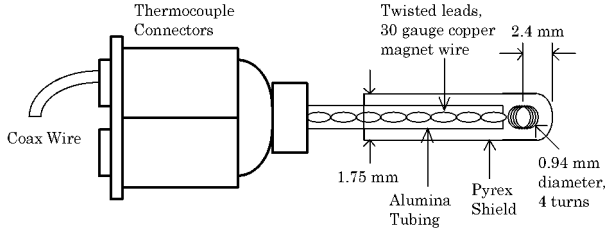

Fig. 5 Magnetic probe schematic.

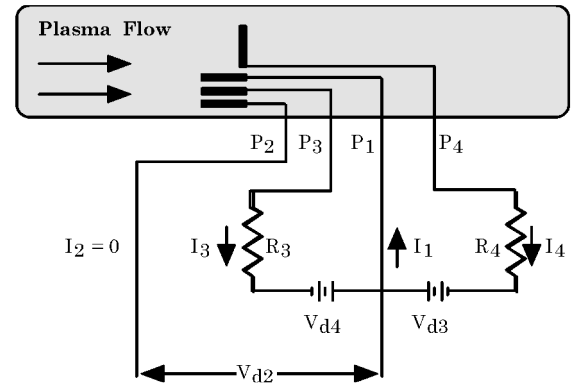

Fig. 6 Quadruple probe circuit schematic.

The enclosed current I_{enc} is evaluated approximately from

$$I_{enc} = \frac{B_\theta l_B}{\mu_0} = \frac{\phi l_B}{\mu_0 n A_{enc}} \tag{3}$$

where l_B is a nearly circular path length of constant magnetic field.

Quadruple Probe Theory

The quadruple probe circuit is depicted in Fig. 6. The electrically floating probe, P_2, assumes the floating potential V_f of the plasma. P_3 and P_4 are biased at $V_{d3} = V_{d4} = 12$ volts negative with respect to P_1 to collect saturation ion currents I_3 and I_4. The probe output consists of the potential of the floating probe V_{d2} relative to P_1 and the time-dependent ion current histories to the biased probes.

Quadruple probe theory is well documented[20,22] and will not be repeated here. This theory is based on operating in a collisionless regime with a thin ion sheath and a Maxwellian electron energy distribution, with corrections made for near-probe collisions.[17]

For a quadruple probe with electrode surface areas $A_1 = A_2 = A_3$ and electrode biasing such that $V_{d3} = V_{d4}$, the electron temperature $T_e(\mathrm{eV}) = 1/\phi$ is calculated from

$$1 = \frac{1 + \exp(\phi V_{d3}) - 2\exp[\phi(V_{d3} - V_{d2})]}{(I_4/I_3)\{\exp[\phi(V_{d3} - V_{d2})] - 1\}} \tag{4}$$

Solved iteratively, Eq. (4) uniquely determines electron temperature as a function of measured quantities V_{d2} and I_4/I_3 and known V_{d2}.

Thomassen and Vondra have detected doubly and triply ionized C and F in the plume of a Lincoln Experimental Satellite (LES)-6 PPT.[23] At the relatively high pressure in this device and the ~2 eV electron temperature, it is assumed that the number of double and triple ions is small; thus, the electron density n_e is calculated for a neutral Teflon plasma ($n_e = n_{C^+} + n_{F^+}$):

$$n_e = \frac{\kappa(I_3/A_3)(1 + I_4/I_3)\exp\left(\frac{1}{2}\right)}{e(kT_e)^{\frac{1}{2}}[\exp(\phi V_{d2}) - 1]}\left(\frac{\sqrt{m_{C^+}m_{F^+}}}{\sqrt{m_{C^+}} + \sqrt{m_{F^+}}}\right) \tag{5}$$

where κ is an electron density correction to account for multiple ion species

$$\kappa = \frac{1 + (n_{F^+}/n_{C^+})}{1 + (n_{F^+}/n_{C^+})(m_{F^+}/m_{C^+})^{\frac{1}{2}}} \tag{6}$$

The ion number density ratio n_{F^+}/n_{C^+} is calculated using the method of Jahn[1] to be 0.034, yielding $\kappa = 0.99$.

The crossed electrostatic probe incorporated into the quadruple probe by way of the perpendicular electrode P_4 provides the ion speed ratio, or Mach number, u_i/c_m, where u_i is the ion directed velocity and $c_m = (2kT_i/\bar{m}_i)^{1/2}$ is the most probable thermal speed of the collected ions. For the case of two equally biased collisionless probes, one probe parallel to the flow axis and one normal, as P_3 and

P_4 are, respectively, the single-species collected ion current ratio for the thin sheath case I_4/I_3 is used to determine u_i/c_m:

$$\frac{I_4}{I_3} = \frac{2}{\sqrt{\pi}}\frac{A_4}{A_3}x_i \exp\left[-\left(\frac{u_i}{c_m}\right)^2\right]\sum_{n=0}^{\infty}\left[\frac{1}{n!}\left(\frac{u_i}{c_m}\right)^n\right]^2\Gamma\left(n+\frac{3}{2}\right) \tag{7}$$

The plasma flowing over the perpendicular electrode induces a wake that prevents a fraction of A_4 from collecting ions. The parameter $x_i = 1/\pi$ represents the geometric fraction of A_4 available for ion collection.[17,20,22]

Probe Measurement Uncertainty

Uncertainty in the quadruple probe measurements of n_e, T_e, and u_i/c_m stems from experimental error in measured quantities as well as systematic error inherent in the probe environment and the quadruple probe theory and its assumptions.

The experimental error in the quadruple probe data corresponds to measurement uncertainties in the probe current, voltage, and geometries. These yield rms experimental uncertainties for n_e (±7%), T_e (±10%), and u_i/c_m (±11%).

Evaluating systematic uncertainties requires evaluation of several plasma length scales. Quasi neutrality is assumed. For the measured conditions at the exit plane of PPT-4 of $n_e = 5 \times 10^{14}$ cm^{-3}, $n_n \approx 10^{16}$ cm^{-3} (Ref. 24), and $T_e = 1.5$ eV, the debye length λ_D is 1.3×10^{-6} cm. The tungsten electrodes have a radius r_p of 0.016 cm. The probe radius/debye length ratio r_p/λ_D is ≈4900, establishing that the thin-sheath assumption is satisfied and that there are no sheath interactions between probe electrodes.

Given singly charged ions and Coulomb collisions, charged particle mean free paths λ_{e-e}, λ_{e-i}, λ_{i-i} are estimated as 969 times the debye length. For ion–neutral and neutral–neutral collisions, the corresponding mean free paths λ_{i-n} and λ_{n-n} are 777 times the debye length.

Charged-particle collisions that serve to affect the collected current must also be considered. The Knudsen numbers (λ_{mfp}/r_p) for electron and ion collisions based on probe radius are = 7.8, above the transition ($Kn \leq 1$) regime where collected current is affected by collisions.

When the end effect parameter $\tau_L = (L_p/\lambda_d)(kT_e/\bar{m}_i)^{1/2}/u_i$ is greater than 50, a cylindrical probe in a flowing plasma will not be sensitive to small-angle misalignments between the electrode and the flow axis.[25] For $u_i \approx 10$ km/s, $\tau_L = 572$, satisfying the >50 condition. In addition, the probe tip collects convected charged particles. From the probe geometry and assumed conditions ($u_i \approx 10$ km/s, $n_i = 5 \times 10^{13}$ cm^{-3}), there is an estimated overstatement of n_e of 11% (Ref. 17), whereas this effect has no significant impact on T_e or u_i/c_m.

From the established uncertainty for n_e, a correction factor $C = 0.89$ is employed to account for collected tip current. Triple probe model assumptions, including the Bohm sheath model and the thin sheath approximation, impart an additional uncertainty of ±50% on the n_e calculation. Theoretical assumptions additionally place an uncertainty of ±10% on the T_e calculation.[26] The total rms uncertainties for n_e, T_e, and u_i/c_m are, thus, 51, 14, and 15%, respectively.

Experimental Results

To increase performance, the PPT was run in the capillary mode, with cavity length 8.3 mm, diameter 4.8 mm, and pulse length to acoustic time ratio $t_p/t_a \approx 4$. The baseline conditions are $E_0 = 9$ J at 1500 V and $\nu = 1.1$ pulses/s, giving 10 W. Additional measurements were made at 5 and 15 J at 1.1 pulses/s.

Heat Measurements

The coaxial geometry of PPT-4 permits approximate measurement of wall heating losses. The PPT-4 thruster head is separated from the capacitor bank by a coaxial stub connector. Thermal losses are determined by measuring the temperature rise rate dT/dt seen by thermocouples fastened to the outside of the aluminum thruster body, the stub connector, and the capacitors.

To quantify the effect of propellant geometry and type on thermal losses, three configurations are used. The thruster is operated in 2-bar and capillary mode with standard Teflon. Additionally, commercial extruded Teflon tubing, which is translucent rather than the opaque white of virgin Teflon, was used in the capillary mode after preliminary tests suggested that radiation through the translucent wall would result in greater thermal losses.

The thermal mass of the thruster head is determined from an inventory of component masses and specific heats. For the thruster head, $\Sigma mc_p = 462$ J/K. For the stub connector, $\Sigma mc_p = 38$ J/K.

The heating rate data were corrected for the axial heat flow along the stainless steel stub connector. The stub heat flow is $\dot{Q}_{stub}$ (W) $= kA_{stub}\Delta T/L_{stub}$ where $kA_{stub}/L_{stub} = 0.036$ W/K.

Measurements were taken at energies $E_0 = 5$, 9, and 15 J in both two-bar and capillary mode configurations. With the thruster pulsing at 1.1 PPS, the temperature rise rate increases slowly and becomes linear (constant dT/dt) after about 100 s. All thermocouple tests performed were for 1000 shots, with additional data taken after the PPT stopped firing until the temperature rise leveled off. Temperature rate measurements were accurate to ±0.015 K/min.

The temperature rise rate is combined with the thermal mass, the heat loss through the stub connector, and a cavity radiative loss to yield the total heating loss $\dot{Q}_{PPT}$. The mean radiative power loss $\dot{Q}_{rad}$ out of the front of the PPT-4 cavity is estimated as 0.4 J/pulse, assuming a 1.5-eV blackbody and a 4-μs pulse.

The heating efficiency η_h, which is the fraction of the energy delivered to the thruster head available for accelerating propellant, is then

$$\eta_h = 1 - \frac{\dot{Q}_{PPT}}{\eta_{tr}E_0\nu} \tag{8}$$

where capacitor-to-arc transfer efficiency η_{tr} is calculated by internal capacitor heating measurements. A heat rise of 0.03 ± 0.01 K/min is measured in the capacitors for the 9-J case, and the thermal mass is estimated to be 2100 J/K, giving 1.1 W in capacitor heating and $\eta_{tr} = 0.89$. This value is in reasonable agreement with a transfer efficiency of 0.86 calculated from the circuit impedances shown in Fig. 2.

The heating power and heating efficiency are listed in Table 1 for the various configurations and energies.

As expected, losses are highest for the 2-bar configurations and the least for the capillary geometries. This is due to the insulator exposure of 33% of the cavity circumference in the 2-bar mode, compared to zero exposure in capillary mode. The most significant result is that 37–74% of the input power is lost as heat for all configurations tested. The translucent capillary, as anticipated, was less efficient than the opaque Teflon under the same operating conditions. The most efficient configuration is the 15-J capillary case with the lowest thermal loss (5.5 W out of 14.6 W). This implies that the PPT may run more efficiently at higher energies.

Thrust and Thruster Efficiency

The performance of PPT-4 was measured to within ±6% at 9 J on the University of Illinois at Urbana–Champaign Compact Thrust Stand[16] using a single-pulse method. Neglecting one shot that was 20% higher than the others, a conservative average impulse bit for

Table 1 PPT-4 thermal power losses

Configuration	E_0, J	$\dot{Q}_{PPT}$, W	η_h
2-bar	5	3.6	0.26
	9	5.7	0.35
	15	9.3	0.37
Capillary			
White	5	2.9	0.41
	9	4.5	0.49
	15	5.5	0.63
Translucent	9	4.8	0.46

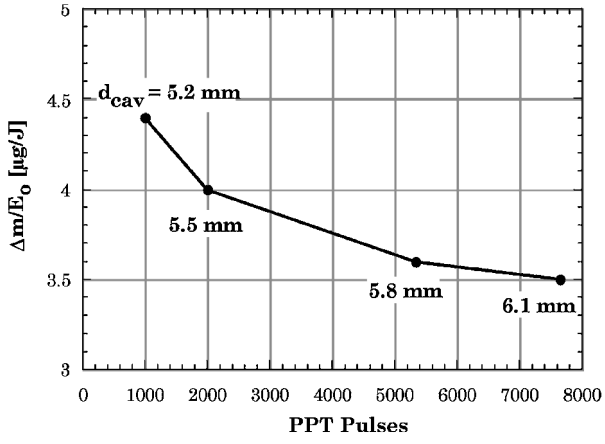

Fig. 7 Average mass loss per Joule vs shots fired; boring out of the Teflon capillary results in a steadily increasing PPT cavity diameter which in turn ablates less mass.

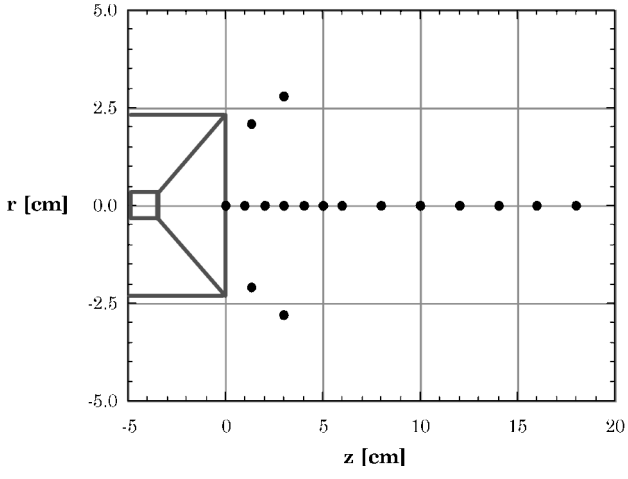

Fig. 8 Quadruple probe probing locations in the plume of PPT-4; 0–180 deg plane is shown, off-axis locations are repeated in 90–270 deg plane.

the remaining pulses is $I_{\text{bit}} = 260 \pm 16$ μN · s. This result also can be expressed as $I_{\text{bit}}/E_0 = 29 \pm 2$ μN · s/J, approximately twice the level achieved by the LES-8/9 PPT operating at 20 J (Ref. 2).

Mass loss measurements indicate a decline in mass loss per pulse per unit energy over time. The results, plotted in Fig. 7, indicate a range of ablation rates. Thrust measurements are taken after ~2000 warm-up pulses. Using a corresponding $\Delta m/E_0 = 3.95$ μg/J/shot gives a thruster efficiency of $\eta_t = 10.6 \pm 1.3\%$ at 9 J. The I_{sp} is 745 ± 45 s.

Quadruple Probe Measurements

The quadruple probe was employed to measure electron density n_e, electron temperature T_e, and ion Mach number u_i/c_m outside the nozzle in the near- and far-field exhaust plume. Attempts were made to probe inside the nozzle, but a change in the shape of the current pulse was observed, suggesting that the current may have been arcing to the probe electrodes.

Measurements were made from $z = 0$ (the exit plane) to $z = +18$ cm along the PPT centerline axis at $E_0 = 9$ J. Off-centerline, or off-axis, measurements were taken by both translating and rotating the probe on the carriage such that the probe was aligned with the plasma flow vector. All probing locations are shown in Fig. 8.

A high-frequency noise signal (~1.4 MHz) was present for all measured probe data, which were of particularly large amplitude during the current pulse, so that data taken during the first 8 μs following ignition were unusable. To reduce noise, a moving-average

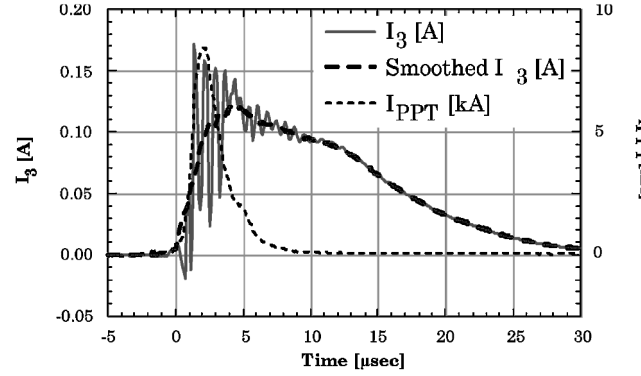

Fig. 9 Comparison of smoothed 10-shot-average data taken at E_0 = 9 J, z = 1 cm to raw 10-shot-averaged data; large amount of noise before t = 8 μs renders that data unusable.

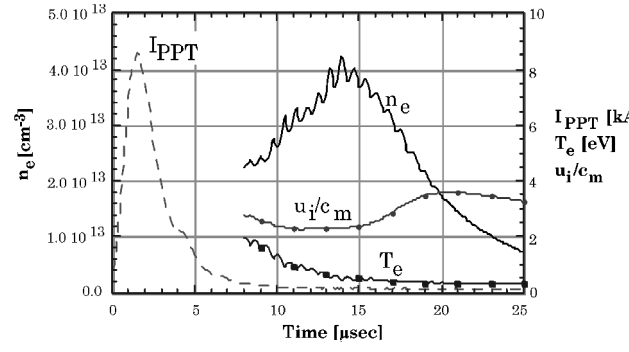

Fig. 10 Typical reduced centerline data from quadruple probe; for this case, z = 3 cm and E_0 = 9 J; although magnitudes and peak times do vary, shapes of curves are relatively constant for all locations and energies.

smoothing routine was applied to a 10-shot average data signal. Sample smoothed probe output is depicted in Fig. 9.

It was also discovered that after ~50 shots, a layer of accumulated Teflon ash deposited on the probes, resulting in a 5–10% decrease in I_3 and I_4. To avoid this problem, the probes were cleaned using ion bombardment before all tests began and following every 30 firings thereafter. The probes were each raised to a potential of 1 kV, and then the chamber was briefly flooded with air through a port directly below the quadruple probe. Once the tank pressure dropped to the Paschen breakdown limit, the electrodes underwent a glow discharge. This discharge was maintained for only a few seconds because longer durations resulted in melting the tungsten wire. Once the cleaning technique was employed, no significant decrease in I_3 or I_4 was discernible under similar operating conditions.

A typical reduced quadruple probe data set is presented in Fig. 10. The case shown corresponds to centerline data at $z = 3.0$ cm and $E_0 = 9$ J. Electron density n_e experiences an initial rise, peaking at $4.2 \pm 1.0 \times 10^{13}$ cm^{-3} at 14 μs, followed by a slow decay. Electron temperature T_e starts at 2.0 ± 0.3 eV at 8 μs, and then slowly cools to about 0.33 ± 0.05 eV at late times. Ion Mach number u_i/c_m maintains a relatively constant supersonic value of 3.0 ± 0.5. Although the magnitudes and peak times do vary for other cases, the shapes of the curves are relatively consistent for all locations and energies.

Peak centerline values of n_e and the times of peak n_e for $E_0 = 9$ J are plotted in Fig. 11 vs distance from the exit plane. A straight-line fit of the n_e peak times from $z = 5$ to 18 suggests an electron/ion velocity of 34 km/s, a value well supported by measurements in rectangular PPTs.[2] A curve fit of the electron density data indicates a peak in n_e occurring at $z \approx 4$ cm. Near-field data for $E_0 = 5$ and 15 J, although insufficient to establish a velocity, indicate a negligible change in n_e for all cases ($n_e \sim 4 \times 10^{13}$ cm^{-3}).

Centerline electron temperature varies very little for the measured probe locations. At E_0 of both 9 and 15 J, T_e starts at 2.0 ± 0.3 eV

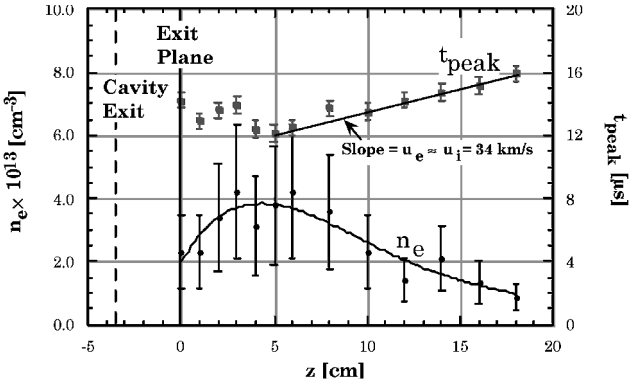

Fig. 11 Peak values of electron density and times of peak density vs distance from exit plane at $E_0 = 9$ J; curve fits illustrate electron/ion velocity and shape of electron density distribution.

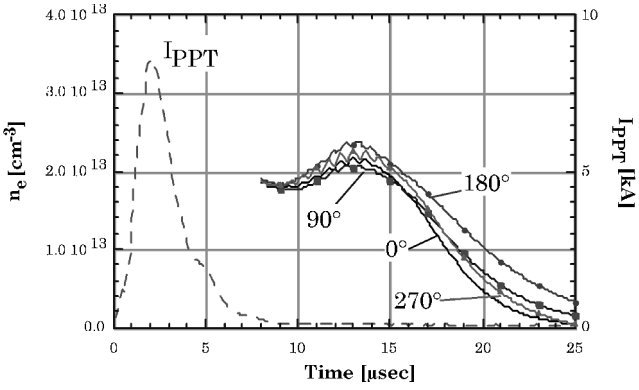

Fig. 12 Off-axis n_e, $E_0 = 9$ J, $z = 1.3$ cm, and $r = 2.1$ cm.

and then steadily decreases to about 0.4 ± 0.06 eV. At $E_0 = 5$ J, T_e typically starts at 1.0 ± 0.2 eV, and drops to 0.4 ± 0.06 eV.

Centerline ion Mach number, similarly, is relatively constant at a supersonic value of 3.0 ± 0.5 with two exceptions. In the far field at $E_0 = 9$ J, u_i/c_m jumps to a hypersonic value of 7.5 ± 1.1. Additionally, at $E_0 = 5$ J, u_i/c_m reaches as high as 5.0 ± 0.8. In both cases, the ions are still at high velocities, suggesting a colder plasma, resulting in a higher Mach number.

Off-axis n_e results at $E_0 = 9$ J, $z = 1.3$ cm, and $r = 2.1$ cm, depicted in Fig. 12, demonstrate remarkable symmetry in the plume at varying values of θ. The measured peak $n_e = 2.1 \pm 0.5 \times 10^{13}$ cm^{-3} is considerably lower than the corresponding interpolated peak value on centerline from Fig. 11 of $n_e = 2.7 \pm 0.7 \times 10^{13}$ cm^{-3}. Farther out in the plume at $z = 3.0$ cm and $r = 2.8$ cm, the electron density drops to $0.2 \pm 0.4 \times 10^{13}$ cm^{-3}, compared with a centerline value of $n_e = 4.2 \pm 1.0 \times 10^{13}$ cm^{-3}. These data suggest a decreasing density distribution across the exit plane and farther out into the plasma.

Also interesting are the off-axis T_e results. The data indicate that the off-axis plasma at $T_e = 1.5 \pm 0.2$ eV is considerably hotter than the centerline plasma ($T_e \sim 0.4$ eV) for the entire 30 μs of data acquisition. At the same time, off-axis ion Mach number data exhibit little variation from the centerline values, remaining relatively constant at a supersonic value of 2.5 ± 0.4 at all probed off-axis locations. It is possible that the off-axis flow is nonequilibrium, as has been found for arcjets.[27]

Ion Mach Number and Velocity

A maximum c_m is calculated by assuming thermal equilibrium: $T_e = T_i \approx 1.5$ eV. This results in $c_m = (2kT_i/\bar{m}_i)^{1/2} = 4.2$ km/s, a value nearly equal to the sound speed for a 1.5-eV Teflon vapor determined by the SESAME code.[28] Centerline and off-axis ion Mach numbers ranging from 2.5 to 7.5 indicate that the ions are traveling from 11 to 32 km/s, values in agreement with published data[2] for rectangular PPTs as well as with the 34 km/s value measured in Fig. 11.

The measured specific impulse $I_{sp} = 745$ s gives a mass-averaged exhaust velocity $u_e = 7.3$ km/s, nearly twice c_m, implying that the nozzle is effectively accelerating the exhaust mass. If late-time ablation, which exhausts heavy Teflon particulates at very low velocities (≤ 0.2 km/s),[9] is taken into consideration, u_e is skewed even higher. The high values of u_i/c_m are encouraging for the continuing development of higher-efficiency PPTs.

Magnetic Probe Measurements

A four-turn, 0.94-mm-diam magnetic probe was used inside the nozzle and in the near-field exhaust plume. Probing proceeded in the nozzle to $z = -25$ mm, where the ratio of the nozzle diameter to the Pyrex probe sheath diameter was ~10:1.

The 99 probing locations in the $\theta = 0$–180 deg plane are plotted in Fig. 13. Data were taken along four equally spaced planes, with the 0-deg plane defined as that containing the igniter plug. All magnetic field data were taken at $E_0 = 9$ J and recorded as an average of 30 PPT firings at each probe location.

A probe calibration yielded nA_{enc} 5% over the geometric value. Uncertainty in data due to shot-to-shot variation is ±12% at low values of B_θ (~30 mT), dropping to 4% for $150 \leq B_\theta \leq 300$ mT.

The most significant conclusion drawn from the magnetic field data is that the PPT-4 plume is not azimuthally symmetric in B_θ, as depicted in Fig. 14, which shows B_θ signals with the Pyrex sheath in contact with the nozzle wall at $r = 8.1$ mm. The smaller signal, peaking at $B_\theta = 150 \pm 6$ mT, occurs at $\theta = 0$ deg, corresponding to the location of the spark plug. The maximum signal, peaking at $B_\theta = 323 \pm 13$ mT, occurs at $\theta = 180$ deg, directly opposite from the plug. The 180-deg signal falls to zero at 4 μs, well before the end of the current pulse.

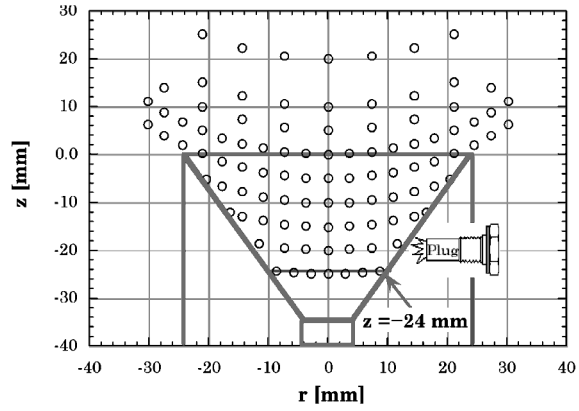

Fig. 13 *B*-probe probing locations in nozzle and plume of PPT-4: 0–180 deg plane is shown, plug location corresponds to positive *r*; all locations are repeated in 45–225, 90–270, and 135–315 deg planes; line at $z = -24$ corresponds to deepest possible penetration into thruster.

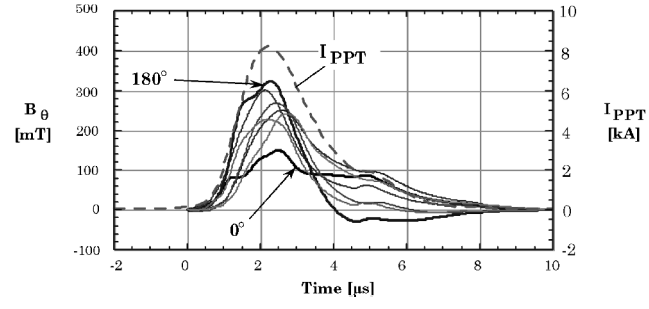

Fig. 14 B_θ signals for $\theta = 0$, 45, 90, 135, 180, 225, 270, and 315 deg at $r = 8.1$ mm (nozzle wall) and $z = 24$ mm; minimum signal occurs at $\theta = 0$ deg, where spark plug is located, peak signal occurs opposite spark plug at $\theta = 180$ deg.

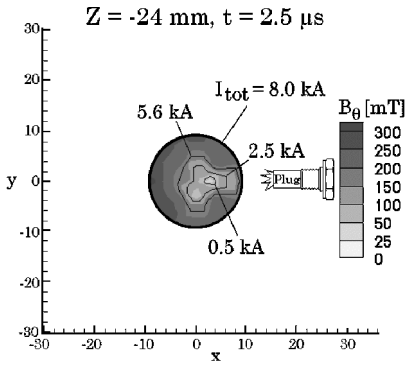

Fig. 15 Contour plot of magnetic field strength B_θ at $z = -24$ mm and $t = 2.5$ μs (near peak current): traces of constant enclosed current I_{enc} are designated as well as total current $I_{tot} = 8.0$ kA; spark plug is at $(x, y, z) = 15.7, 0, -19.1$ mm in the Cartesian system.

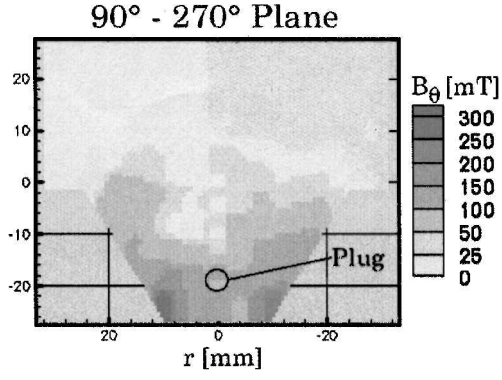

Fig. 16 Side-view contour plot of B_θ at $t = 2.5$ μs (near peak current): spark plug, denoted by a circle, is at $(r, \theta, z) = 15.7$ mm, 0 deg, and -19.1 mm; positive values of r correspond to $\theta = 90$ deg on the plot.

The contour plot in Fig. 15 is the nozzle cross section at $z = -24$ mm and $t = 2.5$ μs, corresponding to a near-peak current of 8.0 kA. The spark plug position in (r, θ) is as indicated, although it is centered at $z = -19.1$, 5 mm forward of the contour plot. Curves of constant enclosed current I_{enc} are designated, as is total enclosed current $I_{tot} = 8.0$ kA. The contours clearly indicate the lack of current symmetry in the system. Data taken farther out in the plume indicate that peak magnetic field decreases to ~150 mT at $z = -15$ and to ~50 mT at $z = 0$.

The side-view contour plot pictured in Fig. 16, which occurs at the same time as Fig. 15, indicate a reflected symmetry about the 90–270 deg plane inside the nozzle of PPT-4. Additional data taken during the pulse show that the 90–270 deg plane symmetry initiates by $t = 1.5$ μs and dissipates by $t = 4.0$ μs, although the total current has decreased to 2.4 kA by this time. There is never any observed symmetry in 0–180 deg plane contours; however, the discussed magnetic field asymmetry deep inside the nozzle is clearly visible.

As discussed earlier, PPT-4 possesses an estimated EM thrust component of 36 μN · s at $E_0 = 9$ J. PPT-4's thrust is dominated by the ET impulse bit, which generates the remaining 86% of the thrust ($I_{ET} = 224$ μN · s). The high degree of symmetry in the quadruple probe measurements indicates that the ET component expands normally about the centerline with no radial ET thrust component.

Even if the EM thrust vector is off-axis as much as 15%, a value not wholly unreasonable considering Fig. 15, the peak radial thrust is 9 μN · s, only 3.5% of the overall thrust.

The data obtained by the magnetic and quadruple probe can be used to calculate the Hall parameter Ω (see Refs. 1 and 17). At the specified plasma conditions, the plasma conductivity $\alpha_0 = 1850\,(\Omega \cdot \mathrm{m})^{-1}$. At a maximum measured magnetic field of 323 mT, the Hall parameter $\Omega = 0.4$, signifying a modest decrease in plasma conductivity from the crossed electric and magnetic fields.

Conclusions

Using a variety of diagnostics, including thermocouples, a thrust stand, a quadruple electrostatic probe, and a magnetic probe, the performance of a coaxial PPT operating in a capillary mode is measured and its plume is explored. Established quadruple probe theory has been modified for the Teflon plasma, and corrections and uncertainties specific to the exhaust density and temperature have been calculated.

Thermocouple measurements indicate that significant thermal losses are present in PPT-4. More than 50% of the terminal power is lost by conduction to the PPT walls in side-fed, 2-bar configurations at any capacitor energy. Running the PPT in capillary mode at higher capacitor energies significantly lessens this trend. Future 2-bar designs must pay particular attention to reducing the exposed insulator surface to reduce this heat loss.

At a standard operating stored capacitor energy E_0 of 9 J and running in capillary mode, PPT-4's average impulse bit, which is 86% electrothermal, is measured to be 29 ± 2 μN-s/J, corresponding to an I_{sp} of 745 ± 45 s, and a thruster efficiency η_t of $10.6 \pm 1.3\%$.

At all tested energies, the quadruple electrostatic probe measures a peak centerline electron density n_e of $4.0 \pm 1.0 \times 10^{13}$ cm^{-3}. Comparison of peak densities at varying probe distances yields an electron/ion velocity of 34 km/s. At $E_0 = 9$ and 15 J, electron temperature T_e reaches a maximum of 2.0 ± 0.3 eV. At $E_0 = 5$ J, T_e peaks at 1.0 ± 0.2 eV. Off-axis quadruple probe measurements indicate excellent symmetry in the plume with lower densities and higher temperatures compared to the centerline values.

A full nozzle and near-field plume survey with the B-probe indicates that the PPT-4 plume is not radially symmetric in B_θ. The radial plume asymmetry corresponds to an radial electromagnetic thrust component, calculated to be 3.5% of the overall PPT thrust.

Acknowledgments

This work was partially funded by the Air Force Office of Scientific Research under contracts F49620-97-1-0138 and F49620-97-1-0443. M. Birkan is the program monitor. Additional support was provided by Naval Research Laboratory (NRL) Grant N00173-98-P-0676 administered by M. Osborn of NRL and E. Pencil of NASA John H. Glenn Research Center at Lewis Field. We also thank R. Spores and G. Spanjers of the Air Force Research Laboratory who provided further support, resources, and counsel, and J. Frus of Unison Industries for his critical support in the development of the external circuit and the igniter system. This work would not have been possible were it not for the machinists who built PPT- 4 and its associated test equipment: S. Sprague, B. Johnson, K. Elam, D. Foley, D. Miller, and D. Tempel. Additionally, we acknowledge the hard work and diligence of students E. Antonsen, F. Rysanek, M. Wilson, J. Norris, M. Morgan, T. Smart, T. Fritz, and J. Konicek.

References

[1] Jahn, R. G., *Physics of Electric Propulsion*, McGraw–Hill, New York, 1968, pp. 1–85, 257–313.

[2] Burton, R. L., and Turchi, P. J., "Pulsed Plasma Thruster," *Journal of Propulsion and Power*, Vol. 15, No. 5, 1998, pp. 716–735.

[3] Akimov, V., Nagel, I., Ogloblina, I., Antropov, N., Pokryshkin, A., Popov, G., and Rudikov, A., "Analysis of PPT Potentialities in Solving the Satellite Orbit Control Tasks," International Electric Propulsion Conf., IEPC Paper 97-146, Aug. 1997.

[4] Ebert, W. L., Kowal, S. J., and Sloan, R. F., "Operational Nova Spacecraft Teflon Pulsed Plasma Thruster System," AIAA Paper 89-2497, July 1989.

[5] Meckel, N. J., Cassady, R. J., Osborne, R. D., Hoskins, W. A., and Myers, R. M., "Investigation of Pulsed Plasma Thrusters for Spacecraft Attitude Control," International Electric Propulsion Conf., IEPC Paper 97-128, Aug. 1997.

[6] Blandino, J. J., Cassady, R. J., and Peterson, T. T., "Pulsed Plasma Thrusters for the New Millennium Interferometer (DS-3) Mission," International Electric Propulsion Conf., IEPC Paper 97-192, Aug. 1997.

[7] Ziemer, J. K., Choueiri, E. Y., and Jahn, R. G., "Scaling Laws for Pulsed Electric Propulsion with Application to the Pluto Express Mission," International Electric Propulsion Conf., IEPC Paper 95-147, 1995.

[8] Myers, R. M., Oleson, S. R., McGuire, M., Meckel, N. J., and Cassady, R. J., "Pulsed Plasma Thruster Technology for Small Satellite Missions,"

NASA CR-1984271995, Sept. 1995.

[9]Spanjers, G. G., Lotspeich, J. S., McFall, K. A., and Spores, R. A., "Propellant Losses Because of Particulate Emission in a Pulsed Plasma Thruster," *Journal of Propulsion and Power*, Vol. 14, No. 4, 1998, pp. 554–559.

[10]Spanjers, G. G., and Spores, R. A., "PPT Research at AFRL: Material Probes to Measure the Magnetic Field Distribution in a Pulsed Plasma Thruster," AIAA Paper 98-3659, July 1998.

[11]Turchi, P. J., Mikellides, I. G., Mikellides, P. G., and Schmahl, C. S., "Theoretical Investigation of Pulsed Plasma Thrusters," AIAA Paper 98-3807, July 1998.

[12]Arrington, L. A., Haag, T. W., Pencil, E. J., and Meckel, N. J., "A Performance Comparison of Pulsed Plasma Thruster Electrode Configurations," International Electric Propulsion Conf., IEPC Paper 97-127, Aug. 1997.

[13]Vondra, R. J., and Thomassen, K. I., "Performance Improvements in Solid Fuel Microthrusters," *Journal of Spacecraft and Rockets*, Vol. 9, No. 10, 1972, pp. 738–742.

[14]Seeglitz, W. G., "A Study of a Cylindrical Pulsed Solid Fuel Microthruster," M.S. Thesis, Dept. of Aeronautics and Astronautics, Massachusetts Inst. of Technology, Cambridge, MA, 1973.

[15]Bushman, S. S., Burton, R. L., and Antonsen, E. L., "Arc Measurements and Performance Characteristics of a Coaxial Pulsed Plasma Thruster," AIAA Paper 98-3660, July 1998.

[16]Wilson, M. J., Bushman, S. S., and Burton, R. L., "A Compact Thrust Stand for Pulsed Plasma Thrusters," International Electric Propulsion Conf., IEPC Paper 97-122, Aug. 1997.

[17]Bushman, S. S., "Investigations of a Coaxial Pulsed Plasma Thruster," M.S. Thesis, Dept. of Aeronautical and Astronautical Engineering, Univ. of Illinois at Urbana–Champaign, Urbana, IL, 1999.

[18]*PSpice Electric Circuit Simulator*, Ver. 5.4, MicroSim, Irvine, CA, 1997.

[19]Cassady, R. J., Meckel, N. J., Hoskins, W. A., Myers, R. M., Oleson, S. R., and McGuire, M., "Pulsed Plasma Thruster Systems for Spacecraft Attitude Control," AIAA Paper 96-2735, Sept. 1996.

[20]Burton, R. L., and Bufton, S. A., "Exit-Plane Electrostatic Probe Measurements of a Low-Power Arcjet," *Journal of Propulsion and Power*, Vol. 12, No. 6, 1996, pp. 1099–1106.

[21]Huddlestone, R. H., and Leonard, S. L. (eds.), *Plasma Diagnostic Techniques*, Academic Press, New York, 1965, pp. 69–112.

[22]Burton, R. L., Delmedico, S. G., and Andrews, J. C., "Application of a Quadruple Probe Technique to MPD Thruster Plume Measurements," *Journal of Propulsion and Power*, Vol. 9, No. 5, 1993, pp. 771–777.

[23]Thomassen, K. I., and Vondra, R. J., "Exhaust Velocity Studies of a Solid Teflon Pulsed Plasma Thruster," *Journal of Spacecraft and Rockets*, Vol. 9, No. 1, 1972, pp. 61–64.

[24]Antonsen, E. L., Burton, R. L., Engelman, S. F., and Spanjers, G. G., "Herriott Cell Interferometer for Unsteady Density Measurements in Small Length Scale Thruster Plasmas," AIAA Paper 2000-3431, July 2000.

[25]Chung, P. M., Talbot, L., and Touryan, K. J., *Electric Probes in Stationary and Flowing Plasmas*, Vol. 2, Springer-Verlag, New York, 1975, pp. 1–38.

[26]Tilley, D. L., Kelly, A. J., and Jahn, R. G., "Application of the Triple Probe Method to MPD Thruster Plumes," AIAA Paper 90-2667, July 1990.

[27]Megli, T. W., Lu, J., Krier, H., and Burton, R. L., "Modeling Plasma Processes in 1-Kilowatt Hydrazine Arcjet Thrusters," *Journal of Propulsion and Power*, Vol. 14, No. 1, 1998, pp. 29–36.

[28]SESAME, *The Los Alamos National Laboratory Equation of State Database, Teflon File 27190*, Los Alamos National Lab., LA-UR-92-3407, Los Alamos, NM, Oct. 1977.